Materials & Design 261 (2026) 115307

Contents lists available at ScienceDirect

Materials & Design

journal homepage: www.elsevier.com/locate/matdes

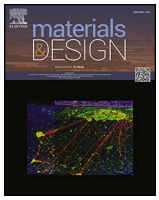

Novel approach to rapid and accurate temperature-dependent mechanical testing using machine learning☆

Akshat Agha *, Janet B. Davis, Sergio L. dos Santos e Lucato

Teledyne Scientific & Imaging, 1049 Camino dos Rios, Thousand Oaks, CA 91360, USA

ARTICLE INFO

Keywords:
Temperature-dependent mechanical properties
Elevated temperature tensile testing
Machine learning in materials science
Full-field strain
Digital image correlation
Rapid testing

ABSTRACT

Understanding the temperature-dependent mechanical properties of metallic alloys is essential for informed engineering design. However, conventional elevated temperature tensile testing is costly, time-consuming, and inefficient. This paper introduces a novel, rapid, and accurate approach for characterizing these properties using a specially designed test sample – MAPS that works at the intersection of full-field optical strain and thermal measurements, and machine learning (ML). The MAPS sample is engineered to exhibit a controlled temperature gradient across its surface, enabling simultaneous acquisition of strain and thermal data at multiple temperatures in a single test. A finite element twin of the MAPS sample is used to generate synthetic training data based on known alloy properties. A Multi-Layer Perceptron (MLP) model is then trained to infer full-field stress distributions from experimental strain and temperature data, allowing the derivation of stress–strain curves across a range of temperatures for novel alloys. The proposed MAPS methodology was validated against conventional dogbone tensile tests conducted on four diverse materials – AA6061-T6, SS301-H12, SS304 and 15-5PH steel. The approach shows good generalizability across material families, showcasing its potential to revolutionize high-throughput temperature-dependent mechanical testing by enabling faster, more cost-effective material characterization for advanced engineering applications.

1. Introduction

Metals are extensively used in high-temperature applications across various industries, such as aerospace, automotive, and power generation. Metallic alloys are specifically engineered to withstand extreme heat while maintaining their structural integrity and performance. However, the critical mechanical properties of metals such as Young's modulus, yield strength, tensile strength and ductility are known to change at elevated temperatures. Understanding their behavior at high temperatures is crucial for material selection, design, and manufacturing to ensure optimal performance throughout their service life.

The global testing standards like ISO 6892-2 [1], EN 2002-002 [2], and ASTM E21 [3] provide guidelines for conducting elevated temperature tensile tests on metallic materials. According to the test standards, high temperature uniaxial tension testing is performed by pulling a dogbone sample on a specialized setup which requires a furnace mounted on a load frame [4,5]. This approach suffers from various problems: (i) multiple repeats need to be performed for every desired temperate level which makes the process cumbersome and inefficient, (ii) clip-on extensometers are challenging to use at high temperatures, impeding accurate strain measurement, (iii) non-uniform temperature distribution on the sample leads to variance and high scatter in the measured properties, (iv) maintaining precise temperature control within the tight tolerance specified by the test standards (e.g. ± 3 °C for temperatures up to 980 °C in ASTM E21) can be difficult, especially at high temperatures. Some researchers [6,7,8] have used custom experimental setups by employing convective ovens with a glass window cutout enabling non-contact strain measurements using digital image correlation (DIC). Such setups have addressed some of the issues in the test standards, but the testing process remains cumbersome and inefficient. These challenges highlight the ongoing need for an improved testing setup that can support rapid material characterization yet ensure accurate and consistent results to enable quick decision-making during the design process.

The advent of machine learning (ML) has created a paradigm shift in almost every industry, and material testing and modeling is no exception. Machine learning has enhanced materials research by automating

☆ This article is part of a special issue entitled: 'AI Materials' published in Materials & Design.

* Corresponding author.
E-mail address: akshat.agha@teledyne.com (A. Agha).

https://doi.org/10.1016/j.matdes.2025.115307
Received 16 June 2025; Received in revised form 23 November 2025; Accepted 8 December 2025
Available online 9 December 2025

data collection, analysis and interpretation of test data, recognizing patterns and accelerating finite element (FE) simulations. [9,10] have used nanoindentation-based experimental results coupled with FE simulations and ML to predict the stress–strain behavior of metallic alloys. [11,12] used a type of feedforward neural network known as a Multi-Layer Perceptron (MLP) to model the stress state dependent fracture behavior of a DP800 steel and AA7075.[13] attempted to estimate the stress–strain curve and r-value of an aluminum alloy using a convolutional neural network on synthetically generated crystallographic images. [14] used deep neural networks with physics-informed feature engineering and physics-informed loss functions to model the creep-fatigue life of 316 stainless steel at elevated temperatures. [15] used machine learning to study the composition design and wear behavior in Al–Cr–Co–Fe–Ni based high entropy alloys.

In the context of high-temperature testing, many researchers have investigated the use of machine learning techniques to model and fit experimental stress–strain curves. In the last decade, several researchers [16,17,18,19,20,21] have shown that ML based models like Artificial Neural Networks (ANNs), Support Vector Machine (SVM), Decision Tree Regression (DTR), and Random forest Regression (RFR) models perform better than the traditionally used polynomial constitutive equations for capturing the temperature and strain dependent stress–strain behavior of metallic alloys while also eliminating the need to calculate a large number of material constants associated with constitutive equations. Most of the existing studies primarily employ machine learning in material data modeling and fitting stress–strain curves obtained through conventional testing techniques. [22] proposed a numerical-experimental method of measuring properties of 12% Cr steels at elevated temperature using digital image correlation and simultaneous thermal measurements. They used temperature gradients on a dogbone like sample to estimate the Young's modulus at a range of temperatures. However, the approach was limited to elastic properties and tested on one material only.

This study presents a rapid and accurate approach to high-temperature tension testing by integrating advanced optical metrology, finite element analysis and machine learning to produce elastic and plastic properties of metals. We propose a unique sample geometry, MAPS that, when coupled with full-field strain and temperature measurements, enables rapid characterization of new materials over a wide range of temperatures by performing inverse analysis using machine learning. The following sections of the paper present the details about the test sample geometry and testing methodology followed by the finite element twin and the development of a machine learning model to demonstrate the MAPS concept. Finally, we validate the testing approach and the ML model on real experimental data for four diverse alloys.

2. Experimental program

2.1. Materials

The testing technique is designed to work with any metal, especially

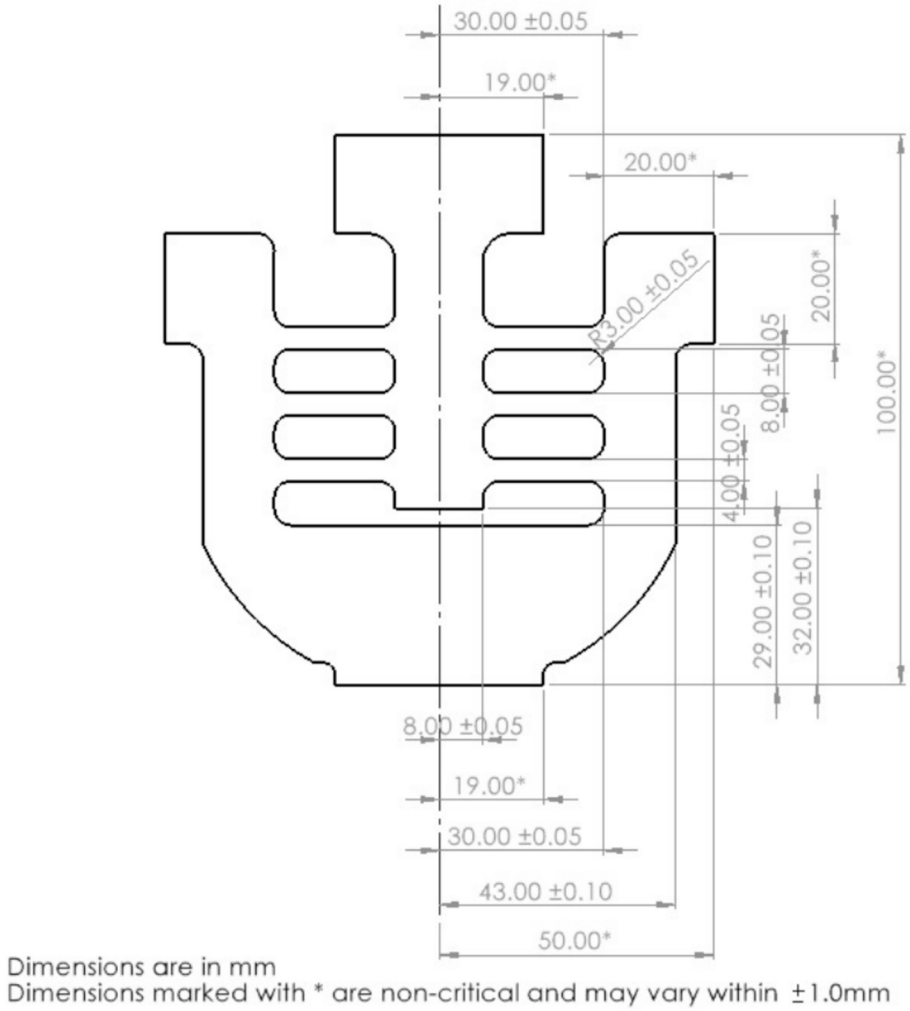

Fig. 1. MAPS test sample geometry.

different grades of steels, aluminum, titanium and nickel alloys. In the scope of this paper, we demonstrate the method using experimental results for four sheet rolled materials: 4.0 mm thick AA6061-T6, 2.6 mm thick SS301-1/2 hard, 3.0 mm thick SS304 and 3.2 mm thick 15-5PH steel.

2.2. Sample geometry

The test sample (shown in Fig. 1) is specially designed to allow measurement of thermo-mechanical properties (Young's modulus, yield strength, ultimate tensile strength and elongation) of metallic alloys. The test sample was designed with several key features to enable comprehensive thermo-mechanical characterization. It facilitates full-field optical strain measurements through digital image correlation (DIC), as well as full-field temperature mapping via infrared (IR) imaging. The geometry of the sample is engineered to produce a controlled temperature gradient across its surface, resulting in locally varying stress concentrations during mechanical loading. To ensure consistent and interpretable results, the sample exhibits mirror symmetry about its vertical axis. The design is compatible with a wide range of metallic alloys, including those produced through rolling, casting, forging, and additive manufacturing. Fabrication is straightforward, utilizing common techniques such as waterjet cutting and conventional machining. Furthermore, the sample is suitable for testing on electro-mechanical or servo-hydraulic load frames equipped with standard wedge grips. To minimize material usage, the test sample was designed with a compact footprint measuring 100 mm × 100 mm.

2.3. Test setup

2.3.1. Load frame

The MAPS approach is carefully designed to work with any standard load frame with appropriate load capacity and mounting grips. For this study, the tests were performed on an MTS servo-hydraulic load frame with a 50 kip (222 kN) static load cell capacity. The machine was equipped with hydraulic wedge grips to mount the test sample. The jaws on the grips were 1.5″ (38 mm) wide, and the grips were provisioned with water cooling to protect the load cell and grips from overheating and obtaining a temperature gradient on the test sample.

2.3.2. Heating

The test sample was heated symmetrically using 4 cartridge heaters – a set of 2 mounted on each side at the heating tabs located at the top of the test sample as shown in Fig. 2 and Fig. 3. The cartridge heaters had a diameter of 0.375″ and were placed inside a custom-built enclosure for easy mounting on the test sample. The heaters had a capacity of 560 Watts (240 V) and were able to heat the test sample to a peak temperature of 600 °C. The heaters had a built-in K-type thermocouple and were controlled by a closed feedback on/off type (binary) temperature control to ensure precise temperature control with a maximum overshoot of 5 °C at the peak temperature. The control unit allowed each pair of heaters (left and right) to be individually controlled to compensate for any misalignments and ensure a symmetric temperature profile on the test sample.

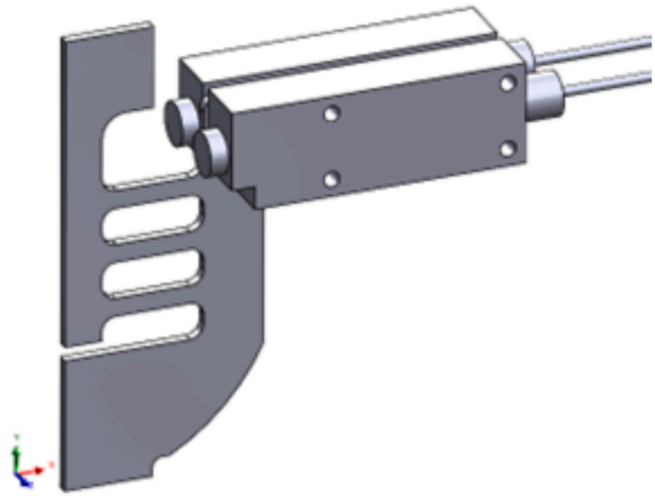

Fig. 2. Schematic showing the cartridge heater enclosures mounted on the test sample.

2.3.3. Strain measurements

The MAPS test sample was painted with a black and white speckle pattern on one side (Fig. 4). The full-field strain measurements were performed using a high resolution 12-megapixels stereo DIC system monitoring the speckle pattern, and the recorded images were processed using the commercial DIC software VIC-3D. The DIC system was calibrated using the etched panels provided by Correlated Solutions. The manufacturer's recommended calibration process was followed. Using this process, the system locks in the position of the left and right cameras and determines the intrinsic camera parameters (like camera angle, calibration deviation, stereo residual, etc.). The relevant DIC hardware parameters are provided in Table 1.

Static noise-floor analysis was performed for the proposed DIC setup and processing parameters. The results showed that average error (lower bound of the noise) was in the order of 0.0005 effective strains with the maximum error being 0.001. The observed error is later used in Section 4.2 for injecting noise in the training data to improve the robustness of the ML model.

Virtual strain gauge study was performed on a MAPS test sample to assess the strain convergence and determine the facet size, step size and strain filter size, which are reported in Table 2. The study confirmed that the strains converge with the mentioned DIC parameters.

2.3.4. Thermal measurements

The thermal measurements were performed using a Teledyne FLIR A700 Infrared (IR) camera. The camera was pointed on the back side of the sample. The back of the test sample was painted with a black paint with calibrated emissivity for accurate temperature measurements. The relevant IR camera parameters are provided in Table 3. A static image of a known length was used to calibrate the length scale of the IR camera and find its spatial resolution.

2.3.5. Synchronization between signals

Using an I/O box, the force measured by the load cell was converted into a 10 V analog signal and sent to the DIC system in real-time. At the start of the test, the DIC system and the thermal cameras were configured to start recording at the same time. This integration ensured a synchronization among the force, strain and temperature measurements from the three different sources.

The test setup is shown in its entirety in Fig. 3.

2.4. Test procedure

First, the MAPS sample with the attached cartridge heaters was mounted on the grips. The grip-to-grip separation at the start of the test was set to 60 mm. When the grips were closed, the test frame was switched to load control to maintain near zero axial load on the test sample.

Next, the heaters were switched on and allowed to reach the set temperature. The temperature on the controller was set to ramp at 50 °C per minute so that the temperature profile on the sample reaches steady state in 8–12 min. The test frame was kept in load control mode during this step to allow for thermal expansion while ensuring no axial forces on the test sample. The thermal profile of the test sample was monitored in

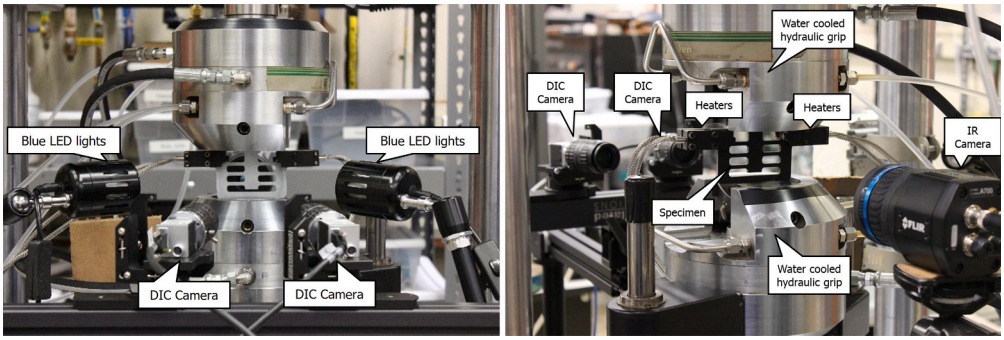

Fig. 3. Front view of the test setup with the MAPS test sample with attached heaters mounted in the grips and the DIC cameras pointed towards the speckle painted side. Back view with the thermal camera pointed towards the black painted side of the sample.

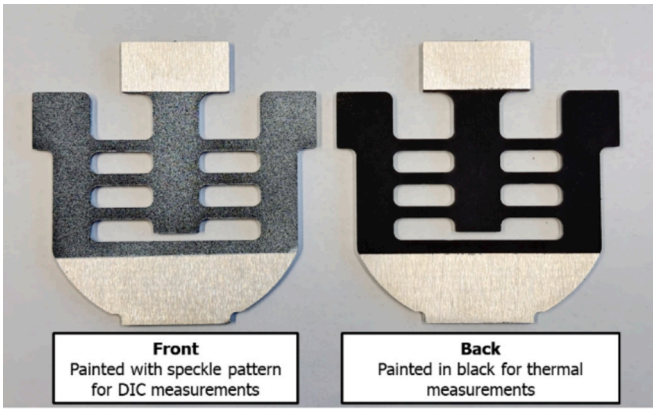

Fig. 4. Front and back side of MAPS sample.

Table 1

DIC hardware	
Camera	Basler 12 megapixels
Lens	Basler 35 mm
Aperture	f/8
Lighting	Blue LED
Image Acquisition Rate	Variable (25 Hz–5 Hz)
Image Resolution	4128 px × 3008 px
Field of View	90 mm × 65 mm
Spatial Resolution	22 μm/pixel
Measuring Distance	280 mm

Table 2

DIC analysis parameters	
Facet size	25 pixels
Step size	5 pixels
Strain filter size	5
Virtual Strain Gauge Length (VSGL)	~1 mm
Matching criterion	Normalized squared differences
Interpolation	Optimized 8-tap spline
Tensor type	Hencky (Logarithmic)
Facet Matching	Combination of reference stage and incremental correlation
Pre-filtering	Low pass filter on images
Post-filtering	None
Software	Correlated Solutions VIC-3D

real time using an infrared (IR) camera. Minor adjustments to the heater temperatures were made to achieve a symmetric thermal distribution across the left and right halves of the sample. To verify symmetry, temperatures at geometrically mirrored locations were compared.

Table 3

IR camera parameters	
Camera	Teledyne FLIR A700
IR Lens	f = 18 mm (24°) F/1.0
Resolution	640 px x 480 px
Field of View	100 mm x 75 mm
Spatial Resolution	156 μm/pixel
Measuring Distance	225 mm
Temperature Scale	0–650 °C
Paint Emissivity	0.93
Software	FLIR Research Studio

Mechanical testing was initiated once the steady-state thermal condition was reached, defined by a temperature variation of less than 5 °C between the left and right halves of the sample.

Once the temperature on the test sample stabilized, the test was started. The crosshead was set to move at a constant speed of 0.1 mm/s pulling the sample at quasi-static strain rate. The DIC system recorded the deformation history with a variable acquisition rate – a higher frame rate of 25 Hz for the first 8 s followed by a slower rate of 5 Hz till the fracture. A higher acquisition rate at the beginning of the test is required to obtain sufficient data points in the elastic regime of the stress–strain curves. In the case of materials with high ductility, the test was stopped at a maximum crosshead displacement of 16 mm.

The MAPS experimental program is designed to cover a wide range of temperatures simultaneously in a single test with redundancy. Since each MAPS test provides data for a wide range of temperatures, only a few tests are sufficient to generate the entire spectrum of stress–strain curves with good certainty. Tests conducted at various heater temperatures result in overlapping temperature ranges. For instance, a test at 100 °C will encompass temperatures from room temperature (RT) to 100 °C, while a test at 200 °C will cover temperatures from RT to 200 °C. Consequently, the predicted data for RT to 100 °C is duplicated across both samples, providing redundancy in the measurements. This feature ensures repeatability in test measurements without the need to perform repeated tests at the same temperature. For this study, the tests were conducted with the heaters set to 25 °C, 150 °C, 250 °C, 350 °C, 450 °C and 600 °C.

2.5. Test data

In this section, we briefly present the test data which consists of a series of DIC generated full-field strain-contour maps, a series of temperature-contour maps and the force vs. displacement plot for the test.

2.5.1. Set of full-field strain-contour maps

The speckle images were processed using DIC analysis parameters given in Table 2 to obtain the components of the planar strain tensor (ε_x,

ε_y and ε_{xy}) at each facet center/node. Since the crosshead displacement recorded by the testing machine includes elastic deformations from components in the load path—such as grips, fixtures, and the machine frame—it does not accurately represent the true local deformation of the specimen. To obtain a more reliable measure of local strain, a virtual extensometer with a gauge length of 35 mm was defined directly on the gauge section of the sample. The resulting force–displacement data was used to validate the finite element (FE) model described in Section 3.2, and for the elasticity MLP model described later in Section 4. The extensometer length was selected arbitrarily but kept consistent across the FE and experimental datasets to ensure comparability. A sample major strain-contour map with the 35 mm virtual extensometer at a displacement of 12 mm is shown in Fig. 5.

As the MAPS sample deforms, the 6 horizontal members start rotating with plastic strain accumulation on the end of each horizontal member near the fillet, and only elastic strains in the rest of the test sample. To investigate the stress state on different sections of the sample, the strains were used to calculate the stress triaxiality. Stress triaxiality is a scalar function of the strain ratio and helps in understanding the stress state [23,12]. A stress triaxiality value of 0.33 denotes uniaxial tension, 0.577 denotes plane strain, 0.667 denotes balanced-biaxial tension, 0 denotes shear and negative values represent the state of compression, and triaxiality values between these indicate mixed loading. The stress triaxiality map shown in Fig. 6 also shows that the regions with the highest strain concentration are under uniaxial tension. The observed behavior is consistent with the beam bending theory and shows a pair of uniaxial tension (yellow) and compression (blue) at the fillet of each horizontal member.

2.5.2. Set of temperature maps

The thermal profile of the test sample was recorded for the entire deformation history. A sample image for a MAPS test at 250 °C is shown in Fig. 7. As per the design requirement, there is a temperature gradient on the test sample with each horizontal member (from top to bottom) at a different temperature. Due to the symmetry built into the test sample and the heater setup, the temperature profile in the left half is similar to the right half. The measurements show that the temperature profile stays consistent during the deformation, and the temperature values stay within 5 °C from beginning to the end of the test.

2.5.3. Force vs. displacement plot

The force recorded by the load frame and the displacement obtained from the 35 mm virtual extensometer constitutes the third important output from the test. Similar to a conventional stress–strain curve for metals, the force–displacement response of a MAPS sample begins with a linear region, followed by transition to nonlinear region that signifies the onset of plastic deformation. A sample Force-Displacement plot for MAPS test is shown in Fig. 8.

A DIC generated video of a MAPS test showing effective strain and temperature distribution on a AA6061-T6 sample at 300 °C heater temperature is provided.

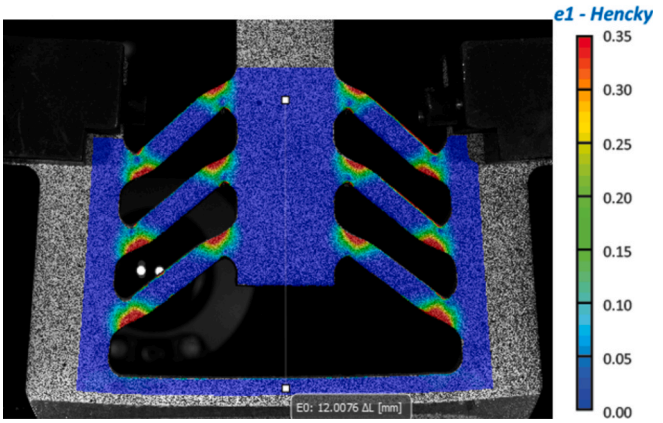

Fig. 5. Full-field strain-contour map generated by DIC overlayed on the image of a speckle painted MAPS sample, and the 35 mm extensometer drawn in the center of the sample.

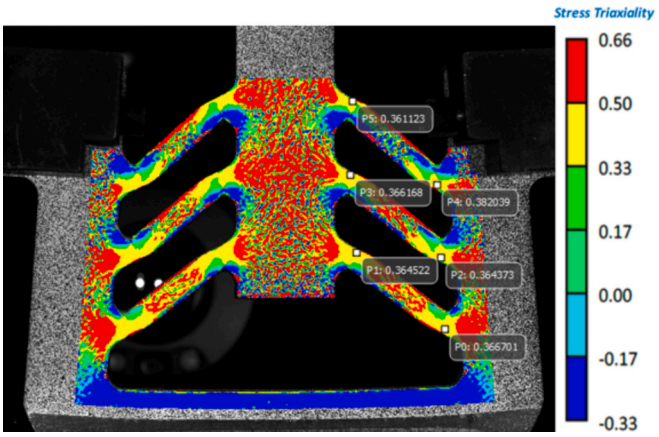

Fig. 6. Stress triaxiality map showing the localized stress state for various locations on the MAPS sample.

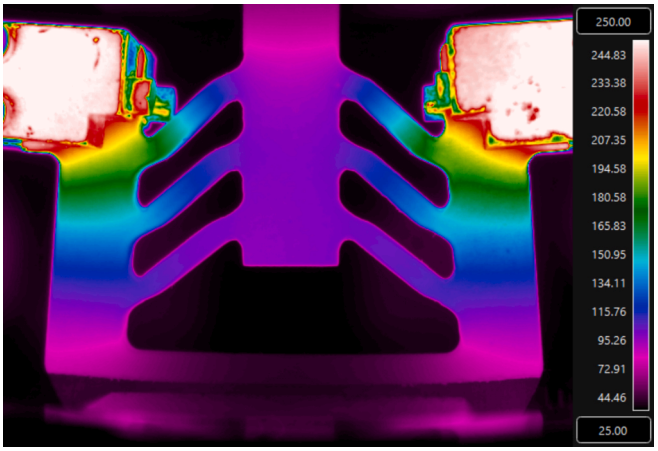

Fig. 7. Temperature-contour map obtained by IR Camera showing a MAPS sample heated to a peak temperature of 250 °C.

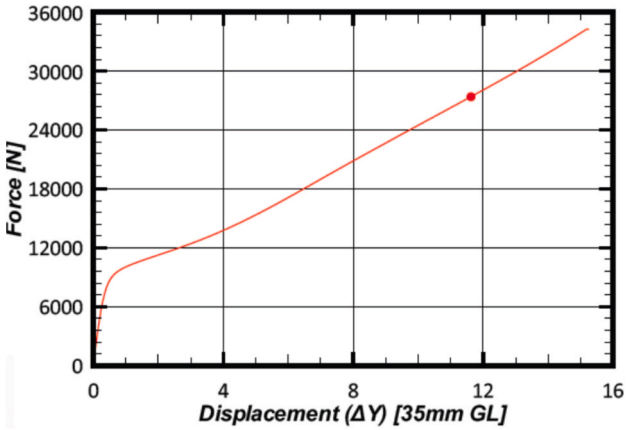

Fig. 8. Sample force vs. displacement plot for a MAPS test.

3. Finite element twin

This section presents the finite element model twin of the MAPS test sample. The goal of the FE analysis was to generate synthetic training data sets of strain, temperature, force–displacement and stresses.

3.1. FE model development

A half-symmetry FE model of the MAPS sample was developed in ANSYS 2024 R2 to mimic the test conditions and obtain training data for the ML model. The model was meshed (30452 elements, 53,884 nodes) using Tet10 solid elements of size 2.0 mm and 0.5 mm with finer mesh at the areas of interest on the horizontal members. The thermal analysis employed SOLID291 elements, with the heating zone surfaces assigned elevated temperatures (set as a parameter in the simulation), while the top and bottom grip regions were maintained at 25 °C to simulate ambient conditions. The resulting temperature distribution from the thermal step was imported as a body load into the subsequent structural analysis, which utilized SOLID187 elements. In the structural step, the top grip surfaces were constrained with fixed boundary conditions, and a displacement was applied in the negative Y-direction to the bottom grip surfaces to simulate uniaxial loading. Fig. 9 shows the mesh, and the boundary conditions for the steady-state thermal and the subsequent static structural step of the simulation.

Temperature-dependent stress–strain curves were provided as an input to the MAPS FE simulation. The curves were either taken from literature [24,25,12,26] or were generated in-house using standard dogbone testing. All the curves were converted to true stress-plastic strain curves and extended using Swift law defined below:

$$\overline{\sigma} = \sigma_0 + K\varepsilon^n \tag{1}$$

MAPS FE data was generated for 12 materials (6 aluminum alloys and 6 steel variants) explained in greater detail in Section 4.2.

3.2. Verification of FE model with experiments

In order to ensure that the FE generated data is in agreement with the experimental data, a thorough verification of the FE model was performed. Two quantities were compared: (i) Experimental vs. FE generated force–displacement profile, (ii) DIC strain vs. FE strain accumulation with time.

There are various factors which can significantly affect the FE model performance and cause mismatch with the DIC strains and force–displacement behavior. Some sources of error in the experiments and FEA and steps taken to mitigate them are described below.

First, the strain computation in DIC involves filtering and smoothing which results in differences in local strain behavior and noise levels. A smaller subset size, step size and filter size allow for very localized strains, but is prone to higher noise and increased uncertainty, whereas larger values for them means that strains are averaged over a larger area which reduces the noise but also loses the resolution for local strains. To mitigate this issue, the spatial resolution, subset size, step size and filter size were appropriately selected to match the Virtual Strain Gauge Length (VSGL) with the FE mesh size.

Second, discrepancies can arise from differences in the spatial locations used for data extraction in DIC and FEA. To standardize the data extraction process, a script was written to enable automated data extraction by selecting and averaging the nodal data lying within a circle of diameter 1 mm centered at the corner of the fillet. Fig. 10 shows the locations of the 6 highly strained regions on each horizontal member; and the FEA nodes, DIC subset centers lying inside the 1 mm circle (horizontal member 3, area 2 shown for example) that are selected for data extraction and modeling.

Third, while DIC provides only the in-plane components of the strain tensor (ε_x, ε_y and ε_{xy}), the FE model yields a full 3D strain tensor with six components. To keep the strain computation consistent across the two sources, the out-of-plane components of the FE strain tensor (ε_z, ε_{yz} and ε_{xz}) were discarded, and the planar components were used to calculate

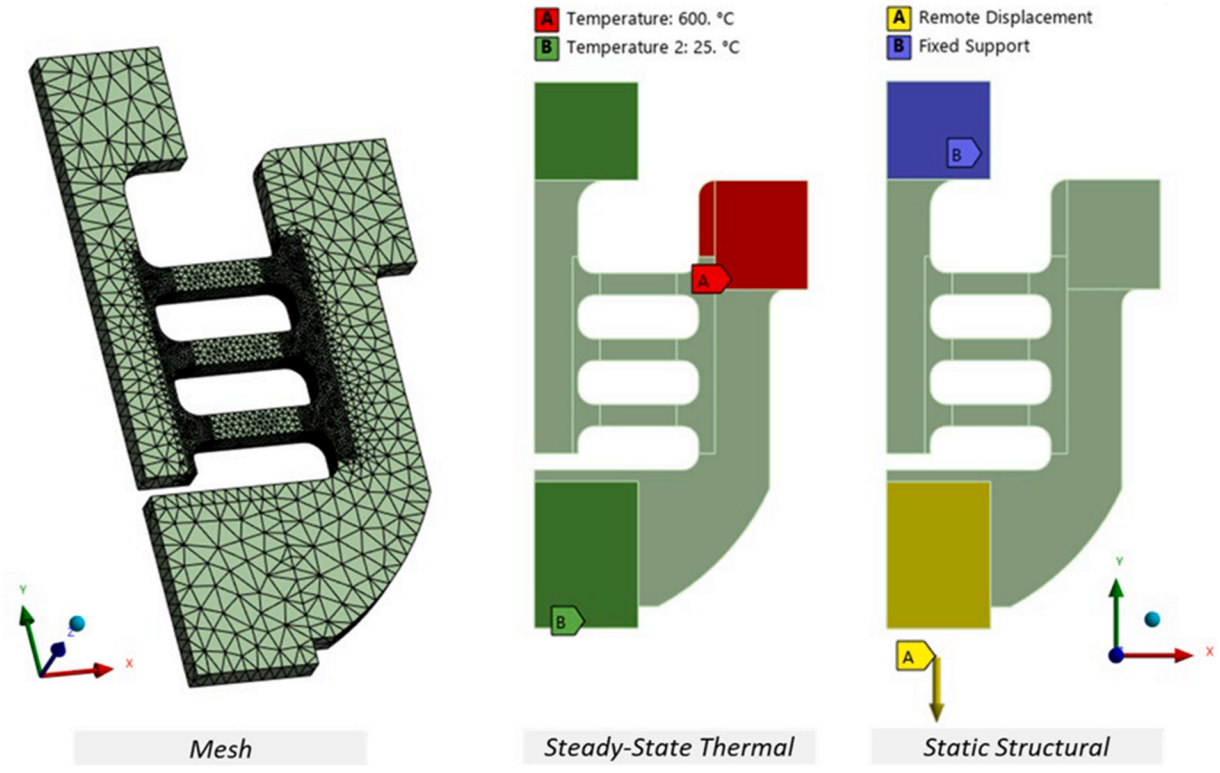

Fig. 9. FE mesh and boundary conditions for steady state thermal step followed by the static structural step.

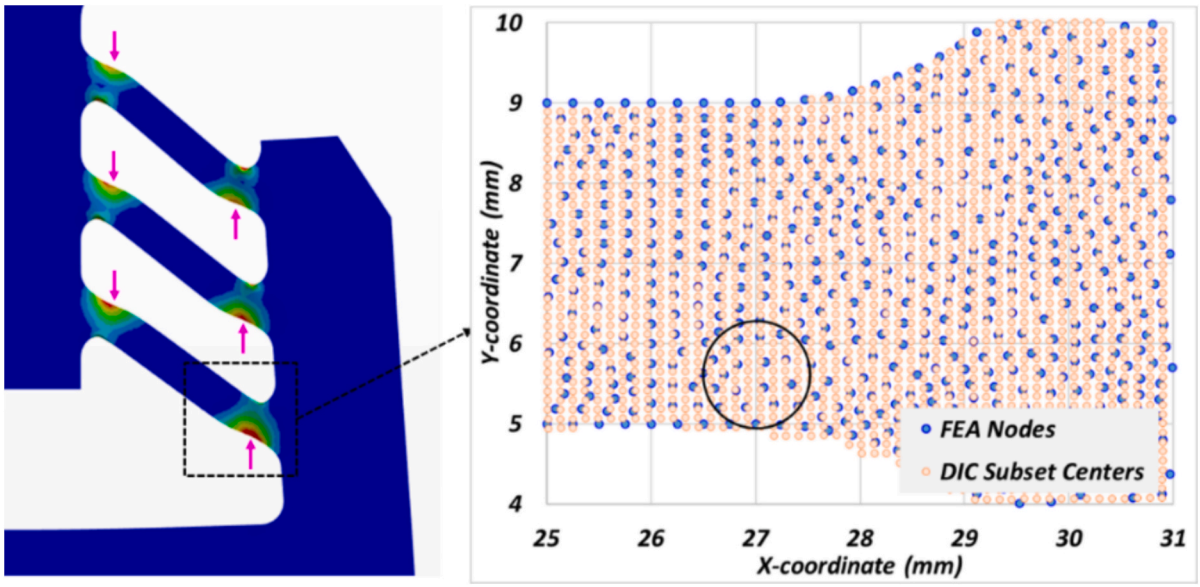

Fig. 10. Map showing the locations of the highly strained regions at the corner of the fillet on each horizontal member; FEA nodes and DIC subset centers inside a 1 mm diameter circle that were selected for data extraction.

the principal stresses (ε_1 and ε_2) which were used to calculate the principal strains and then the von Mises equivalent strain ($\overline{\varepsilon_{VM}}$) using the Eq. (2) given below. The equation was obtained by plugging the volume constancy law $\varepsilon_3 = 0 - (\varepsilon_1 + \varepsilon_2)$ in the von Mises equivalent strain equation.

$$\overline{\varepsilon_{VM}} = \frac{2}{\sqrt{3}}\sqrt{\epsilon_1^2 + \epsilon_2^2 + \epsilon_1\epsilon_2} \tag{2}$$

Additionally, VIC-3D uses a triangle-based strain tensor computation which is a different from the strain computation method used in ANSYS. Matching finite element analysis (FEA) strains with digital image correlation (DIC) strains presents a significant challenge due to the fundamentally different computational approaches underlying each method. FE solvers calculate the strains at the Gaussian points while DIC solves for surface strains. These inherent differences cannot be fully removed; therefore, several strategies were employed to mitigate their impact. Various element types—including solid and shell elements, as well as quadrilateral and tetrahedral meshes—were evaluated against DIC measurements and the Solid tetrahedral elements were found to give results closest to DIC strains. Additionally, mesh refinement was explored, and a solid mesh with a 0.5 mm element size yielded the closest agreement with DIC data. Finer meshes enhance the spatial resolution of strain fields by increasing the number of elements and integration points, thereby improving the accuracy of surface strain interpolation compared to coarser meshes.

The ability to reliably measure small strains with reliability is a well-known challenge for DIC. To minimize this risk, a high-resolution stereo

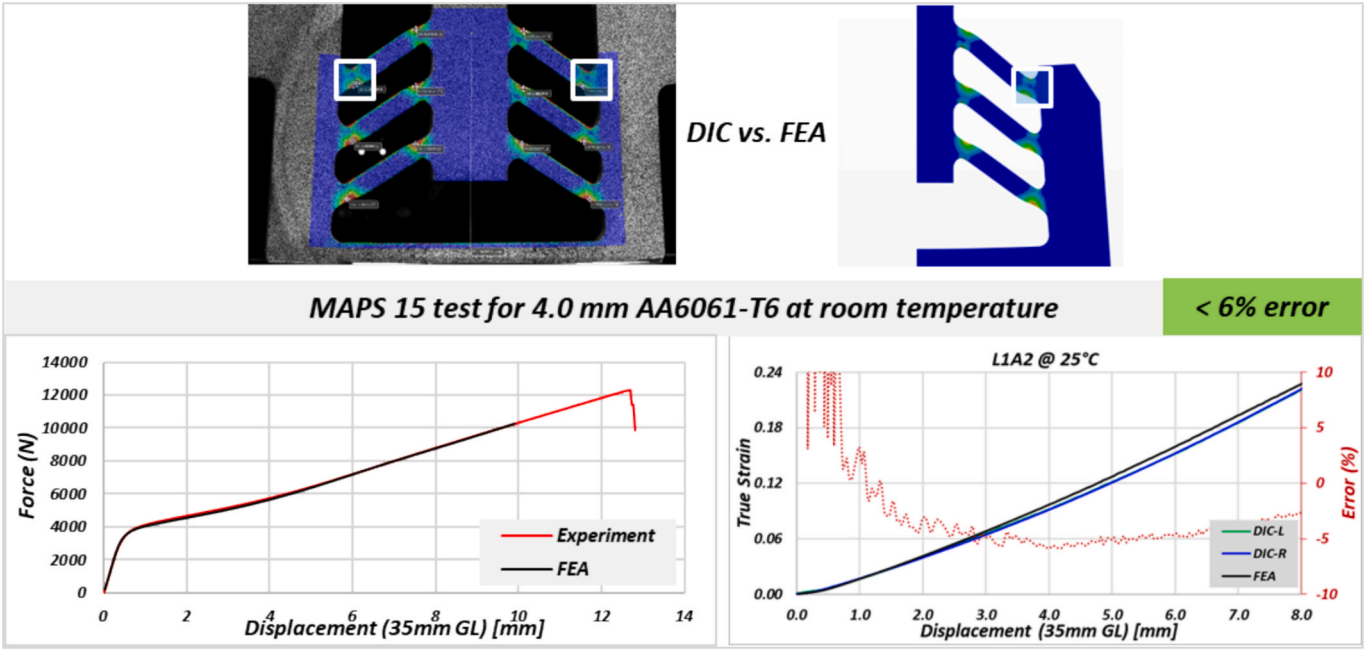

Fig. 11. Top – Location on the MAPS sample used for data extraction from DIC and FEA – Horizontal member 1 (L1) and Area 2 (A2). Bottom Left – Comparison of Force-Displacement plot. Bottom Right- Comparison of effective strains from DIC and FEA.

DIC system was used to achieve a high spatial resolution of 22 μm/px. In addition, the tests were run with variable frame rate with a high image acquisition rate (25 Hz) at the start of the test to obtain more data points (>100 frames) in the elastic regime.

Finally, the force needed to deform the sample is sensitive to the width of the horizontal members and the fillet radius. Hence, it is important to understand and control the geometric variation in the test sample dimensions using tight machining tolerances, shown in Fig. 1.

Fig. 11 shows the comparison plots for the FEA vs. experimentally measured quantities for a MAPS test performed on 4.0 mm thick AA6061-T6 MAPS sample tested at room temperature. The Force vs. displacement curves from FEA and experiment have an excellent match with minimal deviation. The average effective strain inside a 1 mm diameter circle (method of node selection is detailed in Fig. 10) was compared for all the horizontal members. The comparison for the top horizontal member (L1), area 2 (A2) from DIC and FEA is shown as an example in Fig. 11. A good agreement is observed between the corresponding locations on the sample left and right (DIC-L and DIC-R) showing symmetric deformation in the sample. A good agreement is seen between FEA and DIC results with a 6% average error between the effective strain values.

4. Machine learning model

The objective of the machine learning model is to establish correlations between strain and stress across varying temperatures. These relationships are inherently dependent on both the MAPS sample geometry and the material-specific behavior. The degradation of mechanical properties—particularly the reduction in strength at elevated temperatures—varies significantly across and within material families. For instance, aluminum alloys exhibit a more pronounced drop in yield strength at 250 °C compared to steel alloys under the same thermal conditions. This reduction in strength directly influences the force–displacement response observed in MAPS experiments.

The model is designed to interpret the global force measured on a MAPS sample and decompose it into contributions from different material segments on the horizontal members, each experiencing distinct local temperatures. In essence, it aims to resolve the spatially distributed material response under thermal gradients, enabling a prediction of stress based on localized strain-temperature interactions.

In this section, we present a simplistic ML-based model and predict the stresses corresponding to the strain and temperature pairs. We employ a type of feedforward neural network known as a Multi-Layer Perceptron (MLP) to demonstrate the concept.

While DIC measurements are widely accepted for full-field strain measurements, it is well established that their reliability remains limited in the elastic regime – particularly for determining the Young's modulus [27,28,29]. The small strain magnitudes of elastic deformation (typically in the range of 0.001 to 0.0025 for metals) are close to the sensitivity threshold of DIC systems, making them susceptible to noise, and environmental disturbances such as thermal fluctuations.

In our study, we observed that the static noise floor of the DIC setup was approximately 0.001 strains, which significantly compromises the signal-to-noise ratio (SNR) and undermines the reliability of elastic strain measurements. This limitation directly affects the accuracy of elastic modulus predictions. While our plasticity-focused machine learning model operates effectively on localized strain data from the 12 highly deformed regions on the MAPS sample, using these regions to infer elastic properties such as Young's modulus is inherently problematic. To address this challenge, we propose a novel approach that bypasses the use of local strain data by incorporating the 35 mm two-point extensometer, which offers superior SNR and more robust elastic property predictions. Therefore, we split the ML modeling approach into a Plasticity MLP model and a separate Elasticity MLP model.

Both the MLP models were trained using FE-generated synthetic data and then used for predicting stresses in the experimental data. Fig. 12 is a visual representation of the training and prediction approach.

4.1. Plasticity model details

4.1.1. Model architecture for plasticity

For plasticity regime, a MLP with 5 fully connected dense layers is applied to conduct regression analysis. The implementation was done using TensorFlow (an open-source machine learning framework) in

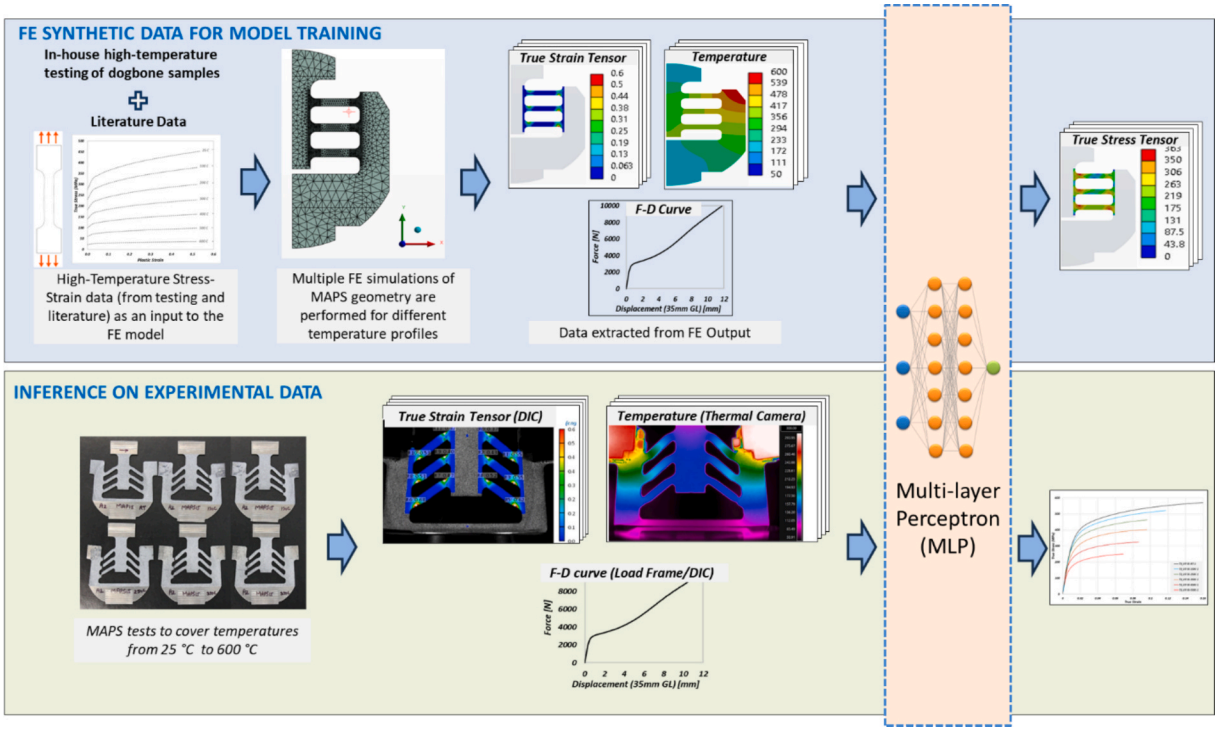

Fig. 12. Representation of the steps taken for training the MLP model using synthetic FEA data and making inferences on the experimental data.

Python. A schematic of the plasticity MLP model is shown in Fig. 13.

- Input Layer: 25 neurons, corresponding to the 25 features of the dataset.
- First Hidden Layer: 256 neurons with ReLU activation.
- Second Hidden Layer: 128 neurons with ReLU activation.
- Third Hidden Layer: 64 neurons with ReLU activation.
- Output Layer: 12 neurons with linear activation which represent the 12 stress values for the corresponding strain-temperature pair.

4.1.2. Training process

- Loss Function: Mean squared error (MSE) was used as the loss function which represents the error in the predicted stresses.
- Optimization: The Adam optimizer was employed with an initial learning rate 0.01.
- Hyperparameters: The model was trained for 300 epochs with a batch size of 32 and a validation split of 20%.
- To ensure optimal model performance and prevent overfitting, a checkpointing mechanism was implemented during training using Keras' ModelCheckpoint callback. This approach monitors the validation loss at the end of each epoch and automatically saves the model weights whenever an improvement is observed. This strategy guarantees that the best-performing model on the validation set is retained for subsequent evaluation and prevents the model to overtrain on the training set.

4.1.3. Evaluation metrics

The model's performance was evaluated using Mean Absolute Error (MAE) and Mean Absolute Percentage Error (MAPE). The validation MAE and MAPE for the best model are 1.996 MPa and 0.69% respectively. The training loss and the validation loss for the 300 epochs are shown in Fig. 14.

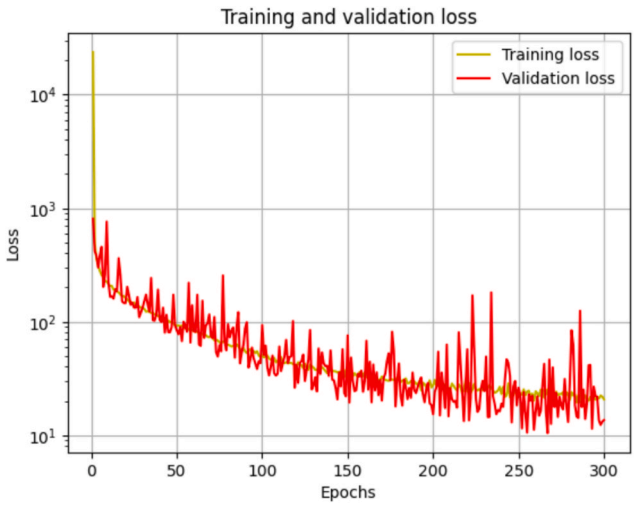

Fig. 14. Training loss and validation loss per epoch for plasticity MLP model.

4.2. Data preparation for plasticity model

The full-field strain-contour on MAPS sample (Fig. 5 and Fig. 6) show that there are 12 highly strained regions on the sample. The other regions on the test sample accumulate purely elastic or significantly low plastic strains. To demonstrate the effectiveness of the testing approach, we utilized the average strains inside 1 mm diameter circle (as explained in Section 3.2) from only the 12 most highly strained locations shown in Fig. 10.

4.2.1. Training data

The training data was generated by running multiple FE simulations of the MAPS sample by changing the material properties and temperature boundary conditions. The model was trained on FE generated synthetic MAPS data for 12 distinct materials. The stress–strain curves for the 6 aluminum alloys (AA2024-T3, AA3003-H14, AA5052, AA6061-T6, AA6063-T6, AA7075-T6) and 6 steel variants (17-4PH-H900, C10, C40, SS304, SS316, SS430) are shown in Fig. 15. The 12 materials were selected to cover a wide range of properties exhibited by the aluminum and steel families. The alloys differ in yield strength, ultimate strength and hardening behavior (slope). It is noteworthy that the alloys exhibit very distinct degradation in response to rise in temperature, especially in the range of 200 °C – 300 °C. The property degradation in aluminum is much severe compared to the steels for the similar temperature range. In addition to the true stress-plastic strain curves, a table of the temperature vs. Young's modulus and Poisson's ratio was also provided as an input to the FE simulations.

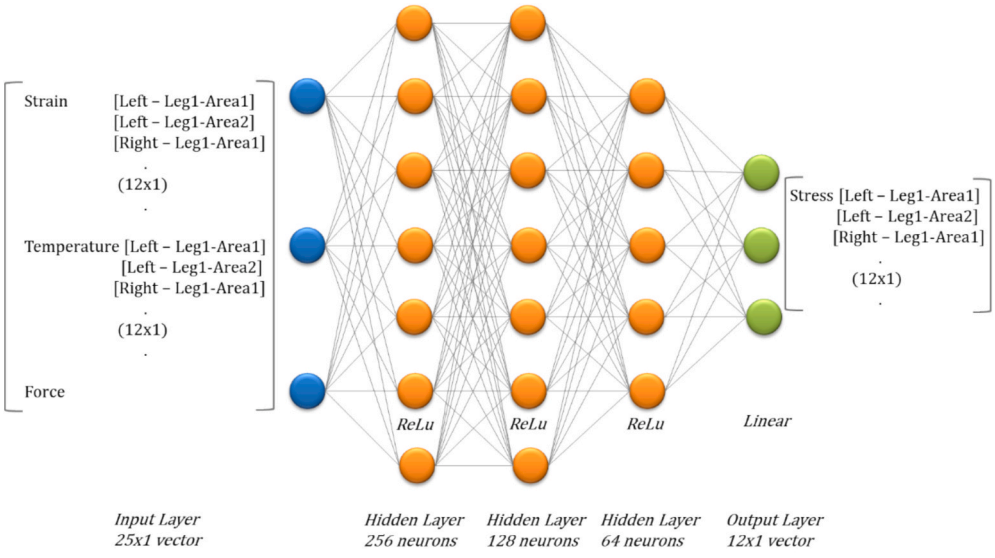

Fig. 13. Architecture of Plasticity MLP model for predicting true stress–strain curves.

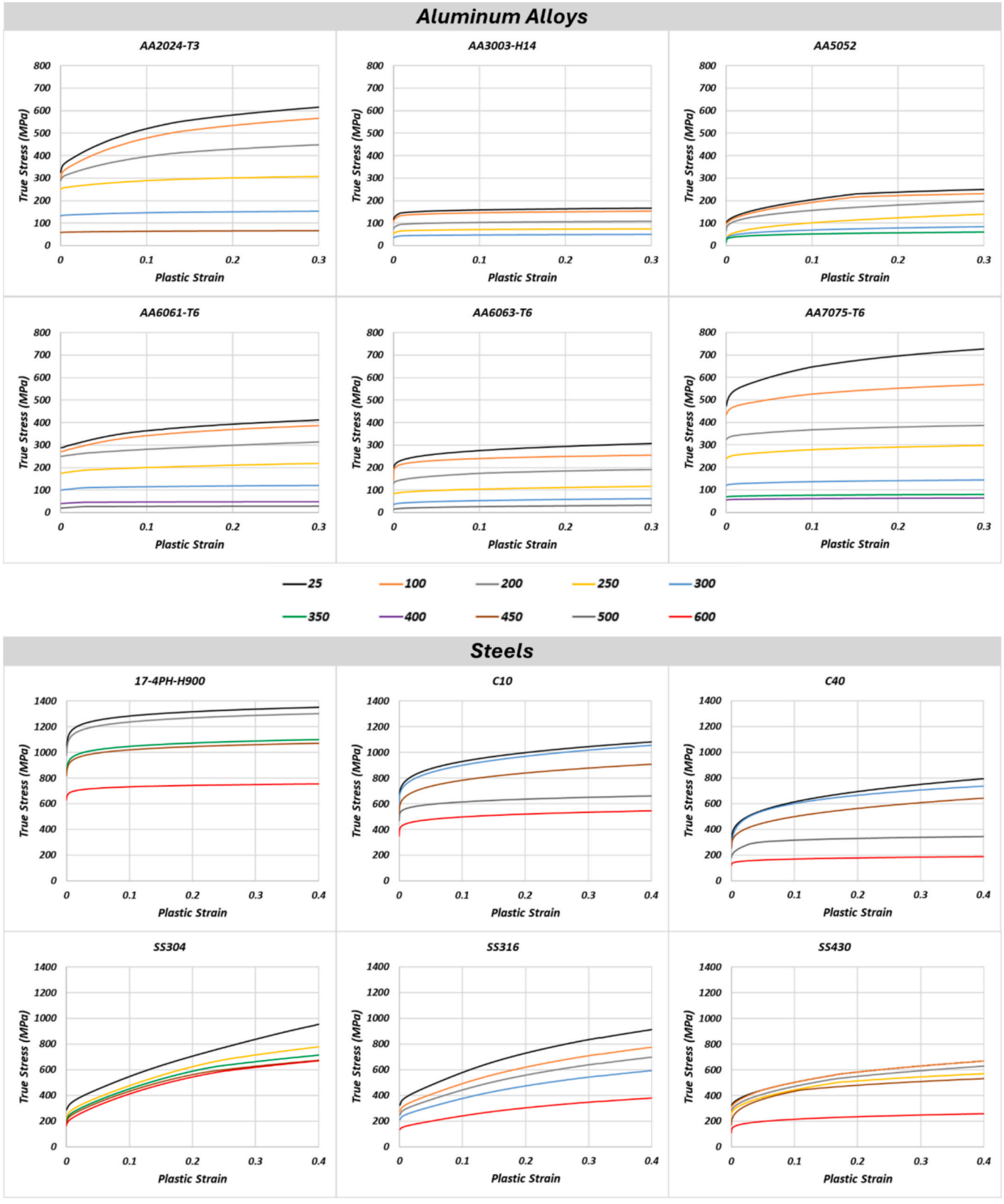

Fig. 15. True stress-plastic strain curves as an input to the MAPS FE model for generating the synthetic training data.

A total of 16 simulations at varying peak temperatures (25 °C, 100 °C, 150 °C, 200 °C, 250 °C, 300 °C, 325 °C, 350 °C, 375 °C, 400 °C, 425 °C, 450 °C, 475 °C, 500 °C, 525 °C and 550 °C) were performed per material. The data was extracted for 287 simulation timesteps from undeformed stage to a final displacement of 10 mm for aluminum alloys and 407 timesteps/16 mm for steels. This resulted in 287 or 407 data pairs for each simulation. Each data pair extracted from FEA consisted of 13 features (6 temperatures, 6 effective strains and global force).

4.2.2. Physics-informed feature engineering

We utilized the understanding of the physical behavior of metals and mechanical testing to enhance the original features of the collected FE data.

Since the FE model was a half-symmetry model, the exported data contained only 6 highly strained regions (assumed as right half of the sample). Although the MAPS test sample is designed to have mirror symmetry, some variation in temperature, strains and stresses is expected during real testing due to the influence of material inhomogeneity, sample manufacturing variations, and measurement errors.

4.2.3. Noise injection and mirror symmetry

The knowledge of error observed in DIC static noise floor and IR measurements was used to inject artificial noise in the FE dataset by introducing a random error in the range (−5 °C to 5 °C) to the temperature, and a random error of (0 to 0.001 strains) to the effective strains. The FE data with induced error was labelled as the data for left half of the sample. This approach increased the number of features to 25 (12 temperatures, 12 effective strains and global force). Additionally, it brought he synthetic FE data closer to the real-world conditions, thereby enhancing the robustness of the ML model.

The MAPS test sample is designed to have plane stress, which results in same stresses on the two faces of the test sample. This behavior along with mirror symmetry was leveraged by adding the mirrored pair of each data point, thereby doubling the sample size. This resulted in 574 data pairs from each aluminum simulation, and a total of 9,184 data pairs for each aluminum alloy. Similarly, there were 13,024 data pairs for each steel.

The global force from the FE simulations corresponded to deformation in half the test sample of thickness 4 mm. The global force in the sample is linearly related to the thickness of the test sample. This understanding of the physical behavior was used to normalize the global force with the sample material thickness and then doubled to represent the actual force which will be observed in testing a full MAPS sample of thickness 1 mm.

In its final form, the input data consisted of 25 features – 12 strains, 12 temperatures and 1 global force with a sample size of 133,312. The output features consisted of 12 equivalent stresses.

4.2.4. Data preprocessing and scaling

The input data features contain strains which lie in the range of 0 to 1, temperature which lies in the range of 25 to 550 and the output feature stress lies in the range of 0 to 1500. To ensure that each feature contributes equally to the model, the data was normalized using Standard scaler by removing the mean and scaling to unit variance.

4.3. Elasticity model details

4.3.1. Model architecture for elasticity

For elastic property prediction, a MLP with 4 fully connected dense layers is applied to conduct regression analysis. The implementation was done using TensorFlow (an open-source machine learning framework) in Python. A schematic of the elasticity MLP model is shown in Fig. 16.

- Input Layer: 7 neurons, corresponding to the 7 features of the dataset.
- First Hidden Layer: 128 neurons with ReLU activation.
- Second Hidden Layer: 64 neurons with ReLU activation.
- Output Layer: 6 neurons with linear activation which represent the 6 Young's modulus values for the corresponding temperatures.

4.3.2. Training process and evaluation metrics

The training process and evaluation metrics were similar to the plasticity MLP model. The elasticity model's performance was also evaluated using Mean Absolute Error (MAE) and Mean Absolute Percentage Error (MAPE) where the validation MAE and MAPE for the best model are 2.04 GPa and 1.02% respectively.

4.4. Data preparation for elasticity model

The input vector for the elasticity model consisted of 6 temperatures from either the left or right halves of the MAPS sample, and slope of the Force-Displacement curve in the linear elastic region. The displacement (in mm) was measured over a 35 mm long 2-point extensometer drawn over the MAPS sample. A Python script was developed to automatically detect the onset of non-linearity in the force–displacement curve. To characterize the linear region, the slope was computed within the force range of 150 N to 50% of the force at the identified onset of non-linearity. This slope was then normalized by the sample thickness prior to being passed to the ML pipeline.

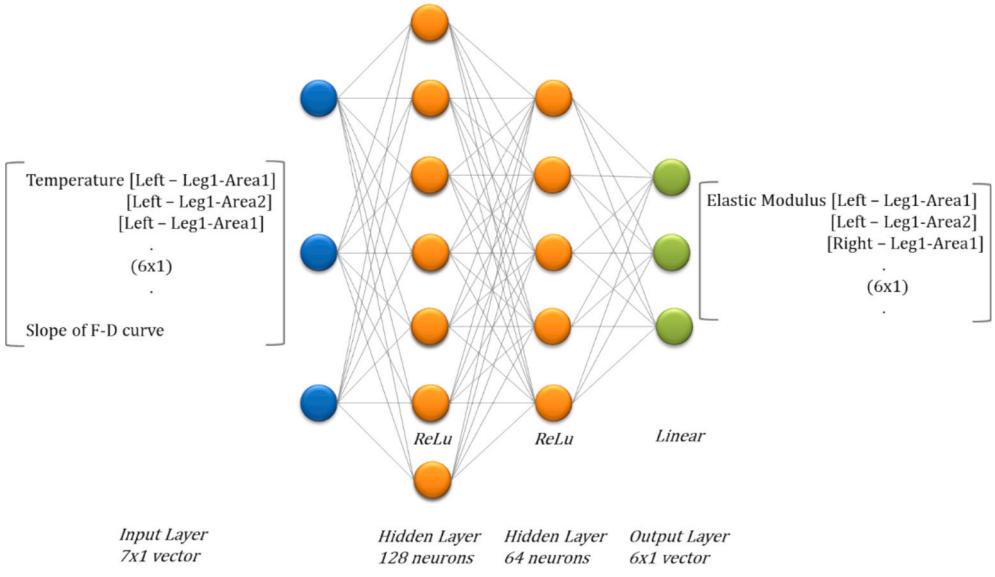

Fig. 16. MLP architecture for modeling the elastic modulus.

The output vector consists of 6 Young's modulus values. For the training dataset, the values were calculated using the ground truth data.

4.4.1. Training data

The 6 temperatures and slope from each FE simulation constituted one data point for the training set. There were 16 data pairs for each material variant, resulting in a total of 384 data pairs for the left and right half of 192 simulations of 12 materials.

4.4.2. Data preprocessing and scaling

To ensure that each feature of the input vector contributes equally to the model irrespective of their absolute value, the data was normalized using Standard scaler by removing the mean and scaling to unit variance.

4.5. Post processing

The plasticity ML model predicts equivalent stresses for each of the 12 strain-temperature pairs, and the elasticity model predicts the Young's modulus values for those temperatures. Since there could be overlapping temperatures in two or more tests, the predicted data for a few temperatures is duplicated across multiple samples, providing redundancy in the measurements. This feature ensures repeatability in test measurements without the need to perform repeated tests at the same temperature.

The stress–strain data and temperature-Young's modulus data predicted by the two ML models from the set of samples tested at different temperatures is consolidated and then grouped by temperature, with the temperatures rounded to the nearest multiple of 25 °C. For example: temperatures from 87.5 °C to 112.4 °C would be rounded to 100 °C. Then an average and standard deviation is calculated per temperature. This method helps in simplifying the data analysis by reducing the number of distinct temperature values, grouping the predicted data for all the test samples and making it easier to identify trends and calculate uncertainty in the prediction. The predicted stress–strain curves and Young's modulus values are not fit to any constitutive model and left as point clouds to show the predicted output in its truest form.

5. Results

To assess the generalization of the proposed ML models, we implemented a two-fold validation scheme. First, we performed a one-material hold-out study where the model was trained on all material except one and then evaluated on the excluded material. Second, we validated the model performance over real experimental data for 1 aluminum and 3 steel alloys and compared the model output with ground truth stress–strain curves. This experimental validation provides a rigorous test of the model's predictive accuracy under real-world conditions and across distinct material classes.

5.1. One-material hold-out study

The first step in the evaluation of the ML model was to understand its ability to generalize for unseen material variants. The study involved training the model on all materials except one and subsequently evaluating its performance on the material that was left out.

For quantifying the predictive accuracy of the ML model in the one-material hold-out study, we report the Mean Absolute Percentage Error (MAPE) for each held-out material. MAPE provides an intuitive measure of error, particularly useful for comparing performance across different materials, as it normalizes the error relative to the magnitude of the stresses for individual material variants. The results of the one-material hold-out study for both the models are shown in Fig. 17.

5.1.1. Plasticity MLP model

In general, the MAPE values for all the steels are lower than 5% except for 17-4PH-H900, and the MAPE for all the aluminum alloys is lower than 10% except for AA3003-H14. A closer examination of the mechanical properties shown in Fig. 15 reveals that AA3003-H14 (MAPE 15%) corresponds to the lowest magnitude of stresses in the dataset, while 17-4PH-H900 (MAPE 8%) represents the highest. These are the materials that lie at the extreme ends of the property distribution in the training set. Overall, the model performs exceptionally well when interpolating within the range of stresses observed in the training data but shows a slight decline in accuracy when extrapolating beyond the stress range in the training set.

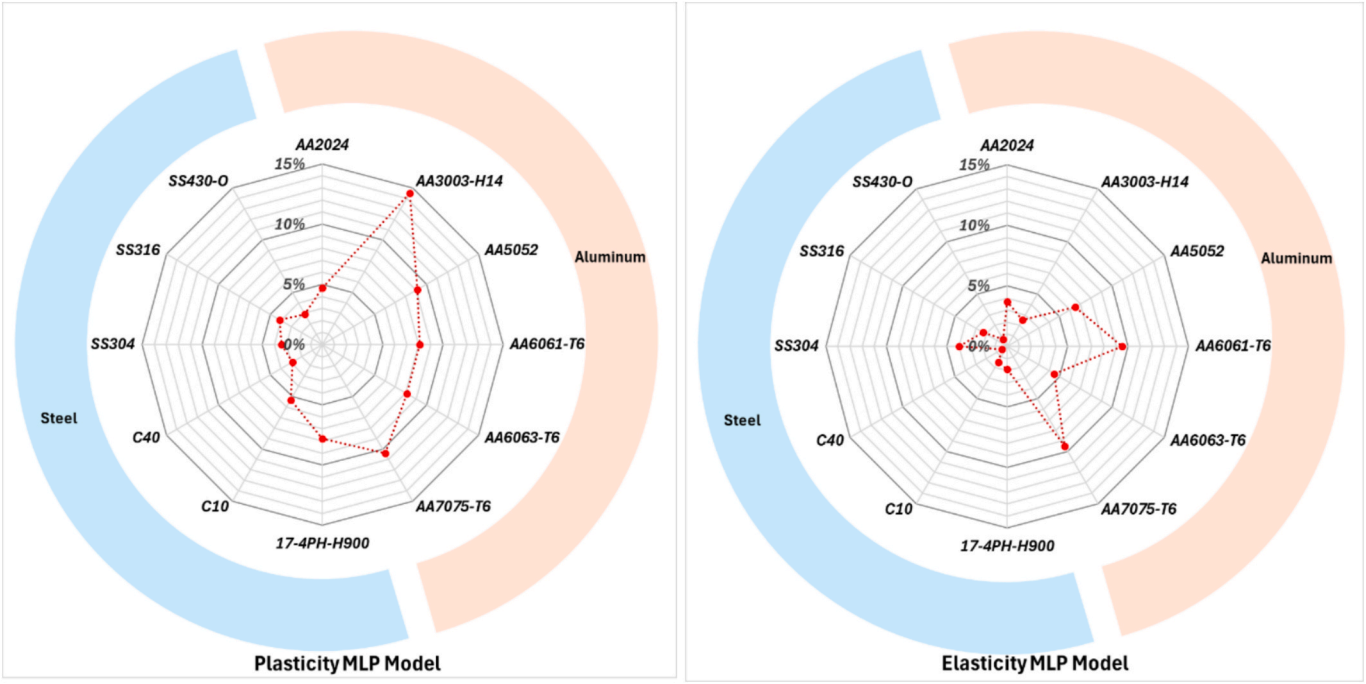

Fig. 17. Results of one-material hold-out study showing the MAPE for material variants.

5.1.2. Elasticity MLP model

The Young's modulus values for most of the cases lie within 5% MAPE and within 10% MAPE for all the cases. The model performs worse on the aluminum than steel.

In a nutshell, the models perform well in the one-material hold-out study and the low MAPE values demonstrate the models' ability to generalize beyond the materials included in training. The study also provides confidence that the models' learned relationships are transferable across alloys from different families – aluminums and steels.

5.2. Experimental validation

The second step of validation involves using real experimental data from MAPS tests and using it to predict stress strain curves and elastic modulus from the ML models. The elastic and plastic mechanical properties predicted by the MAPS approach were compared to the elevated temperature stress–strain data obtained from conventional dogbone tests. The validation was performed on 1 aluminum alloy and 3 steel variants: AA6061-T6 that is a popular aluminum alloy widely used across several industries including aerospace, automotive, marine and construction, Stainless steel 301-1/2 hard known for its high yield strength and fatigue resistance, Stainless steel 304 which is one of the most widely used stainless steels because of its excellent corrosion resistance, low yield combined with significant strain hardening and ductility and 15-5PH steel which is a precipitation-hardening martensitic stainless steel known for its high strength and toughness used in high-performance applications. The chosen materials differ significantly in their behavior and cover a wide range of properties.

5.2.1. AA6061-T6

The MAPS samples were waterjet cut from a 4.0 mm thick cold rolled sheet of AA6061-T6 manufactured by Arconic, USA. 5 samples were tested at heater temperatures 25 °C, 150 °C, 250 °C, 350 °C and 500 °C. The synchronized strain, displacement data from the DIC, temperature data from the IR camera and the force data from the load frame were used to infer the stresses, elastic modulus from the ML models. The force value was normalized for the sample thickness before taking inference from the ML model.

The model output contains the stress–strain curves for every temperature from 25 °C to 400 °C. Here we show the predicted stresses (moving average) for specific temperatures and the envelope of standard deviation in Fig. 18. The ground truth curves used for comparing the results were obtained from the Granta Materials database. The literature-based ground truth properties used for validation may differ slightly from those of the tested sheet. It is known that material properties can vary based on factors such as coil characteristics, thickness, rolling process parameters, tempering process parameters, etc.

The true stress-plastic strain curves are within 10% of the ground truth data for most of the temperatures and within 15% for the worst case. The Young's modulus values are well within 10% of the ground truth values. The predicted stress–strain curves appear wavy as they are not smoothened or fit to any constitutive model to show the predicted output in its truest form.

5.2.2. SS301-1/2 hard

MAPS samples were waterjet cut from 2.6 mm thick rolled sheets of SS301-H12 manufactured by United Performance Metals, USA. 5 samples were tested at heater temperatures 25 °C, 150 °C, 250 °C, 350 °C, 450 °C and 600 °C. The test data was run through the ML pipeline and stress–strain curves and elastic modulus were predicted. The ground truth data for plastic regime was tested in-house using dogbone samples on a conventional setup, whereas the ground truth elastic modulus was obtained from Granta Material database. The comparison of the MAPS results and ground truth data is shown in Fig. 19.

The model performs well on this material and the stress prediction are within 5% of the ground truth data. The Young's modulus predictions show a systematic bias, and all the predicted values are underestimated by 12–15%.

5.2.3. SS304

MAPS samples were waterjet cut from 3.0 mm thick rolled sheets of SS304 manufactured by Outokumpu, USA. 4 samples were tested at heater temperatures 25 °C, 250 °C, 450 °C and 600 °C. The test data was run through the ML pipeline and stress–strain curves and elastic modulus were predicted. The ground truth data for plastic regime was tested in-house using dogbone samples on a conventional setup, whereas the ground truth elastic modulus was obtained from Granta Material database. The comparison of the MAPS results and ground truth data is shown in Fig. 20.

The model predicted stresses lie within 10% of the ground truth data. The Young's modulus predictions follow the same trend and are in general underestimated by 10–12%.

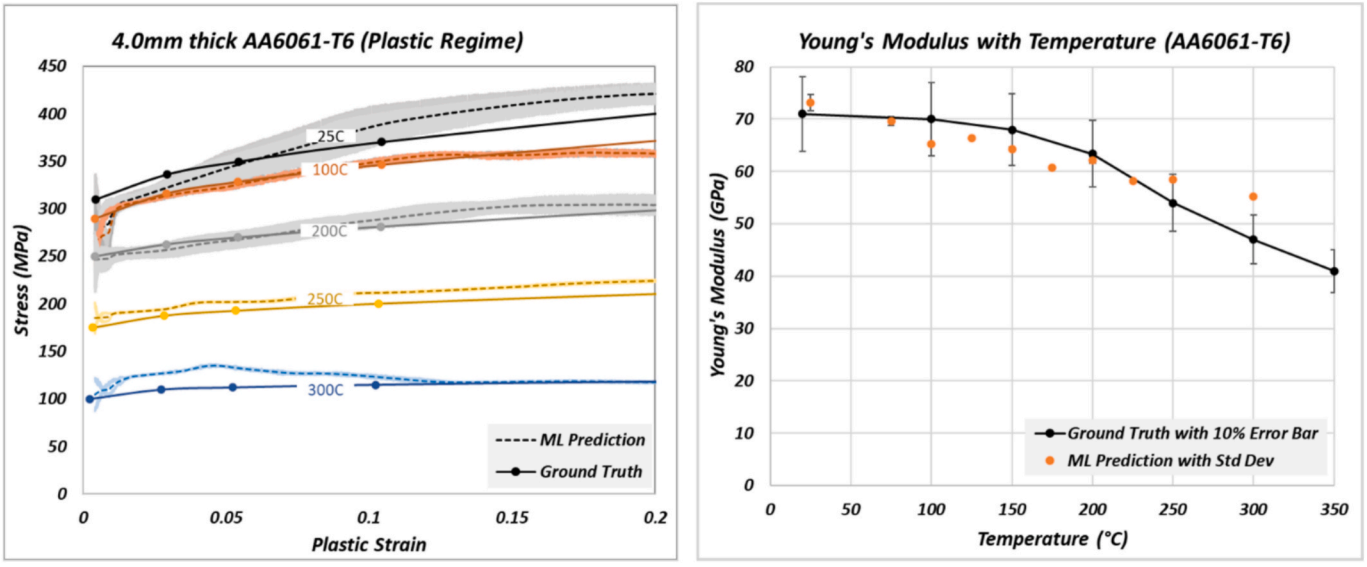

Fig. 18. Stress-Strain curves and Young's Modulus along with the standard deviation envelope predicted by ML model using MAPS experimental data, overlayed on the ground truth data for AA6061-T6.

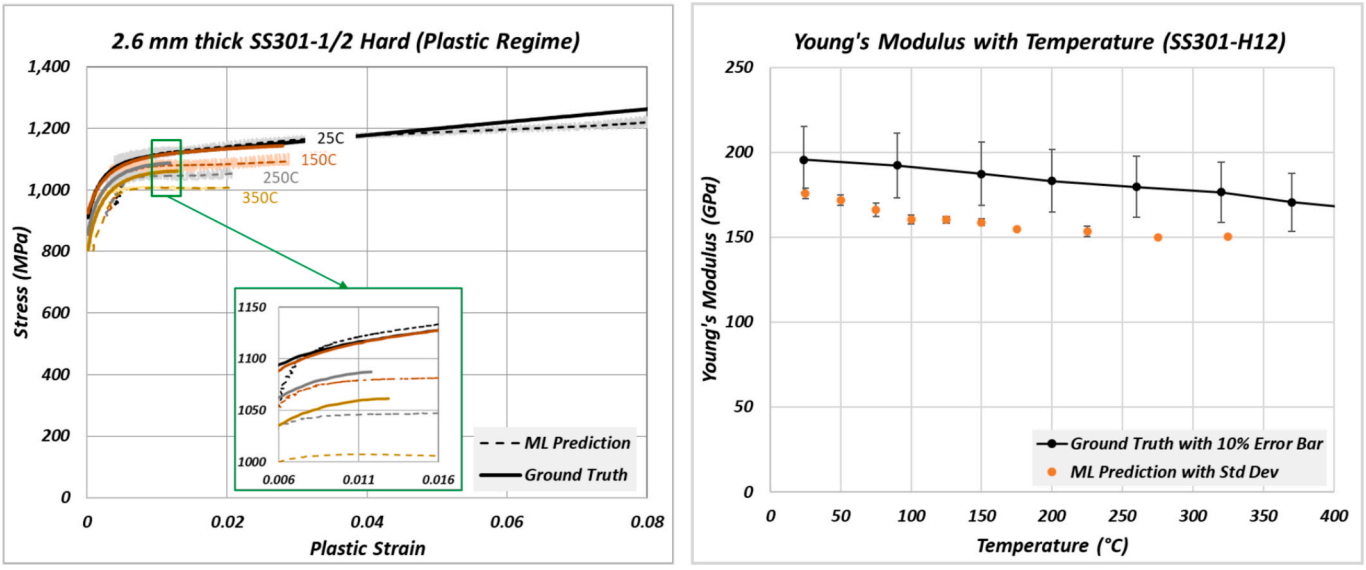

Fig. 19. Stress-Strain curves and Young's Modulus along with the standard deviation envelope predicted by ML model using MAPS experimental data, overlayed on the ground truth data for SS301-1/2 Hard.

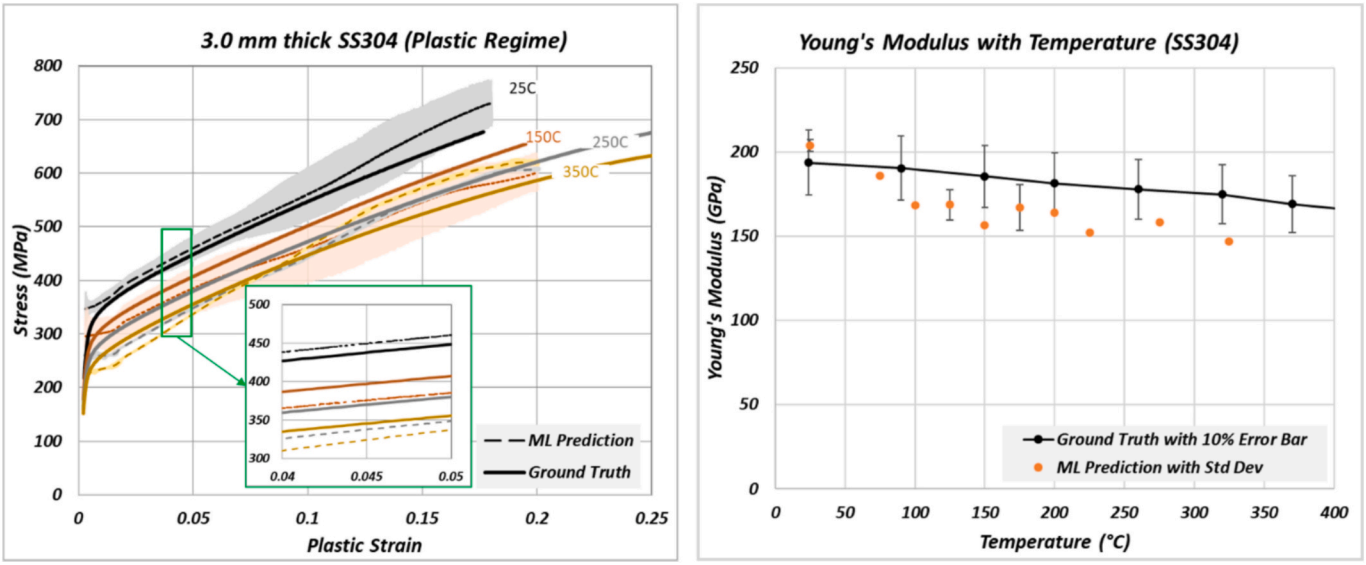

Fig. 20. Stress-Strain curves and Young's Modulus along with the standard deviation envelope predicted by ML model using MAPS experimental data, overlayed on the ground truth data for SS304.

5.2.4. 15-5PH

MAPS samples were waterjet cut from 3.2 mm thick rolled sheets of 15-5PH stainless steel, procured from the vendor Grainger Industrial Supply, USA (unknown manufacturer). 6 samples were tested at heater temperatures 25 °C, 150 °C, 250 °C, 350 °C, 450 °C and 600 °C. The comparison of the MAPS results and in-house tested dogbone samples on a conventional setup is shown in Fig. 21.

The model predicted stresses lie within 5% of the ground truth data. The Young's modulus predictions are underestimated but lie within 10% of the ground truth properties.

6. Discussion

The MAPS approach, as presented, demonstrates strong performance across a wide range of aluminum and steel alloys. It effectively captures material behavior and trends for previously unseen materials using MAPS experimental data. The model achieves an average MAPE of under 10% for both plastic stress–strain curves and elastic modulus predictions.

One of the biggest risks for the work was to get the strains from FEA to match with experimental DIC strains. In the FE model verification at room temperature shown in Section 3.2, we had observed a 6% average error in DIC strains compared to the FE strains. While it is acknowledged that strain measurement vs. FEA errors at elevated temperatures can reach or even exceed 6%, the resulting error in stress predictions (which is an accumulation of strain measurement error, misalignments, ML modeling errors etc.) remains below 10%, as demonstrated in Section 5.2. This is primarily because stress values in the plastic regime are less sensitive to small variations in strain. For example, if the true stress at 2% strain is 500 MPa, a measurement error resulting in 2.1% strain does not proportionally increase the stress to 550 MPa. Thus, a 5% error in strain typically translates to a smaller percentage error in stress, making the stress predictions more reliable despite the inherent strain uncertainties.

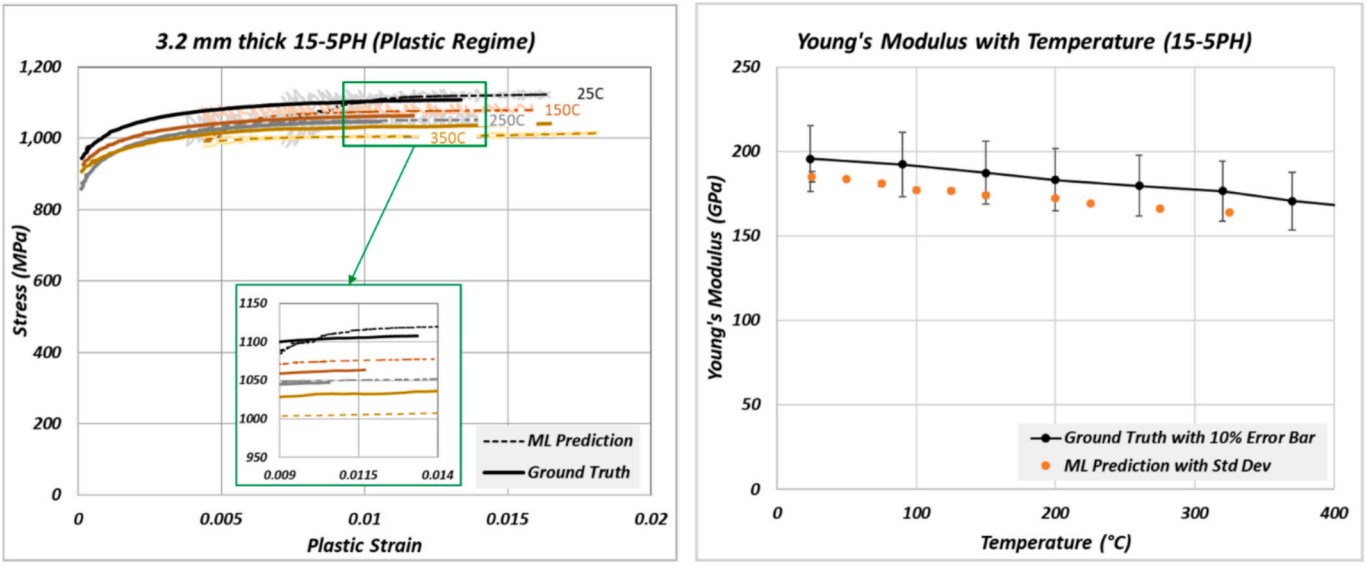

Fig. 21. Stress-Strain curves and Young's Modulus along with the standard deviation envelope predicted by ML model using MAPS experimental data, overlayed on the ground truth data for 15-5PH.

Notably, even a simple MLP model yields promising results, underscoring the robustness of the MAPS methodology. To validate the concept, we currently utilize only point cloud data from 12 regions of the test sample. However, the MAPS test sample contains a full-field strain contour, which holds significant potential for training more advanced, image based neural networks and physics-informed machine learning models. Incorporating such models—capable of leveraging full-field data and physics-based loss functions—is expected to enhance stress prediction accuracy. This direction will be explored further in future work.

The approach is capable of generating mechanical properties over a range of temperatures using only a few samples (4–6 MAPS samples) as seen in the experimental validation, which is much faster and efficient compared to conventional testing which involves testing multiple samples at discrete temperatures. Therefore, the MAPS approach offers a rapid yet accurate method of determining mechanical properties at elevated temperatures.

7. Conclusion

In this paper, we presented a novel testing approach for measuring the temperature-dependent mechanical properties of metallic alloys. The proposed testing approach uses a novel sample that works at the intersection of state-of-the-art optical extensometry, full-field thermal measurements and machine learning to predict temperature dependent stress–strain curves. The technique involves full-field strain measurements using stereo DIC and temperature measurements using an IR camera. The test sample features easy mounting and testing on standard testing load frame with wedge grips. The approach enables accurate temperature-dependent mechanical property measurements while simplifying the test approach and significantly dropping the quantity of samples required for testing. The system provides a table of temperature-dependent Young's modulus and plastic stress–strain curves (presented here as plots) which can be directly used as an input in FE solvers.

To demonstrate the concept, we trained simple multi-layer perceptron (MLP) models using synthetic FE data and validated the performance on real experimental data for 4 materials belonging to aluminum and steel families. The MAPS testing methodology shows great potential for evaluating the temperature-dependent properties of conventional as well as novel alloys across material systems.

8. Project Funding

This work was supported by the Defense Advanced Research Projects Agency (DARPA) contract HR0011-24-C-0392, Multiobjective Engineering and Testing of ALloy Structures (METALS). The views, opinions, and/or findings contained in this article are those of the authors and should not be interpreted as representing the official policies, either expressed or implied, of DARPA or the Department of Defense.

CRediT authorship contribution statement

Akshat Agha: Writing – original draft, Validation, Methodology, Investigation, Formal analysis, Conceptualization. **Janet B. Davis:** Funding acquisition, Conceptualization. **Sergio L. dos Santos e Lucato:** Writing – review & editing, Resources, Project administration, Funding acquisition, Conceptualization.

Declaration of competing interest

The authors declare that they have no known competing financial interests or personal relationships that could have appeared to influence the work reported in this paper.

Acknowledgements

We would like to express our gratitude to Dr. Alex Wagner and Dr. Derek Eidum from Teledyne Scientific & Imaging and Dr. David B. Marshall from University of Colorado, Boulder for their valuable advice and insights. Their contributions significantly enhanced the quality of this work. We would also like to thank Dr. Jun Hu from Cleveland-Cliffs for providing several grades of steel for preliminary testing, which was instrumental in finalizing the experimental approach.

Appendix A. Supplementary data

Supplementary data to this article can be found online at https://doi.org/10.1016/j.matdes.2025.115307.

Data availability

Data will be made available on request.

References

[1] ISO. ISO 6892-2:2018 - Metallic materials — Tensile testing — Part 2: Method of test at elevated temperature 2018. https://www.iso.org/standard/72571.html (accessed April 3, 2025).

[2] CEN. CSN EN 2002-002 - Aerospace series - Metallic materials - Test methods - Part 2: Tensile testing at elevated temperature 2002. https://www.en-standard.eu/csn-en-2002-002-aerospace-series-metallic-materials-test-methods-part-2-tensile-testing-at-elevated-temperature/ (accessed April 3, 2025).

[3] ASTM. Test Methods for Elevated Temperature Tension Tests of Metallic Materials 2020. https://doi.org/10.1520/E0021-20.

[4] J. Chen, B. Young, Stress-strain curves for stainless steel at elevated temperatures, Eng. Struct. 28 (2006) 229–239, https://doi.org/10.1016/j.engstruct.2005.07.005.

[5] M. Knobloch, J. Pauli, M. Fontana, Influence of the strain-rate on the mechanical properties of mild carbon steel at elevated temperatures, Mater. Des. 49 (2013) 553–565, https://doi.org/10.1016/j.matdes.2013.01.021.

[6] A. Agha, F. Abu-Farha, Numerical implementation and validation of a viscoelastic-plastic material model for predicting curing induced residual stresses in adhesive bonded joints, Int. J. Adhes. Adhes. 118 (2022) 103195, https://doi.org/10.1016/j.ijadhadh.2022.103195.

[7] Y. Du, J. Peng, Zhan, J.Y. Richard Liew, Li G. Qiang, Mechanical properties of high tensile steel cables at elevated temperatures, Constr. Build. Mater. 182 (2018) 52–65, https://doi.org/10.1016/j.conbuildmat.2018.06.012.

[8] Q. Zheng, T. Furushima, Evaluation of high-temperature tensile behavior for metal foils by a novel resistance heating assisted tensile testing system using samples with optimized structures, J. Mater. Sci. Technol. 94 (2021) 216–229, https://doi.org/10.1016/j.jmst.2021.03.061.

[9] P.G.M. Flávio, L.R.C. Muniz, T. Doca, ANN strategies for the stress–strain analysis of metallic materials: Modeling, database, supervised learning, validation and performance analysis, Finite Elem. Anal. Des. 230 (2024), https://doi.org/10.1016/j.finel.2023.104097.

[10] J. Weng, R. Lindvall, K. Zhuang, J.E. Ståhl, H. Ding, J. Zhou, A machine learning based approach for determining the stress-strain relation of grey cast iron from nanoindentation, Mech. Mater. 148 (2020), https://doi.org/10.1016/j.mechmat.2020.103522.

[11] X. Li, C.C. Roth, D. Mohr, Machine-learning based temperature- and rate-dependent plasticity model: Application to analysis of fracture experiments on DP steel, Int. J. Plast 118 (2019) 320–344, https://doi.org/10.1016/j.ijplas.2019.02.012.

[12] K.S. Pandya, C.C. Roth, D. Mohr, Strain rate and temperature dependent fracture of aluminum alloy 7075: Experiments and neural network modeling, Int. J. Plast 135 (2020), https://doi.org/10.1016/j.ijplas.2020.102788.

[13] K. Koenuma, A. Yamanaka, I. Watanabe, T. Kuwabara, Estimation of texture-dependent stress-strain curve and r-value of aluminum alloy sheet using deep learning, Mater. Trans. 61 (2020) 2276–2283, https://doi.org/10.2320/matertrans.P-M2020853.

[14] X.C. Zhang, J.G. Gong, F.Z. Xuan, A physics-informed neural network for creep-fatigue life prediction of components at elevated temperatures, Eng. Fract. Mech. 258 (2021), https://doi.org/10.1016/j.engfracmech.2021.108130.

[15] L. Qiao, J. Zhu, Cuckoo search-artificial neural network aided the composition design in Al–Cr–Co–Fe–Ni high entropy alloys, Appl. Surf. Sci. 669 (2024) 160539, https://doi.org/10.1016/J.APSUSC.2024.160539.

[16] U.M. Chaudry, R. Jaafreh, A. Malik, T.S. Jun, K. Hamad, T. Abuhmed, A comparative study of strain rate constitutive and machine learning models for flow behavior of AZ31-0.5 Ca Mg alloy during hot deformation, Mathematics 10 (2022), https://doi.org/10.3390/math10050766.

[17] M. Karimzadeh, M. Malekan, H. Mirzadeh, N. Saini, L. Li, Hot deformation behavior analysis of as-cast CoCrFeNi high entropy alloy using Arrhenius-type and artificial neural network models, Intermetallics (barking) 168 (2024), https://doi.org/10.1016/j.intermet.2024.108240.

[18] M. Murugesan, J.H. Yu, K.S. Jung, S.M. Cho, K.S. Bhandari, W. Chung, et al., Supervised machine learning approach for modeling hot deformation behavior of medium carbon steel, Steel Res. Int. 94 (2023), https://doi.org/10.1002/srin.202200188.

[19] P. Opěla, J. Walek, J. Kopeček, Machine learning techniques in predicting hot deformation behavior of metallic materials, CMES – Comput. Model. Eng. Sci. 142 (2025) 713–732, https://doi.org/10.32604/cmes.2024.055219.

[20] O. Sabokpa, A. Zarei-Hanzaki, H.R. Abedi, N. Haghdadi, Artificial neural network modeling to predict the high temperature flow behavior of an AZ81 magnesium alloy, Mater. Des. 39 (2012) 390–396, https://doi.org/10.1016/j.matdes.2012.03.002.

[21] H. Shang, P. Wu, Y. Lou, J. Wang, Q. Chen, Machine learning-based modeling of the coupling effect of strain rate and temperature on strain hardening for 5182-O aluminum alloy, J. Mater. Process. Technol. 302 (2022), https://doi.org/10.1016/j.jmatprotec.2022.117501.

[22] M. van Rooyen, T.H. Becker, High-temperature tensile property measurements using digital image correlation over a non-uniform temperature field, J. Strain Anal. Eng. Des. 53 (2018) 117–129, https://doi.org/10.1177/0309324717752029.

[23] A. Agha, Effectiveness of 2D digital image correlation in capturing the fracture behavior of sheet metal alloys, SAE Internat. J. Mater. Manuf. 16 (2022), https://doi.org/10.4271/05-16-02-0009.

[24] J. Li, F. Li, J. Cai, R. Wang, Z. Yuan, F. Xue, Flow behavior modeling of the 7050 aluminum alloy at elevated temperatures considering the compensation of strain, Mater. Des. 42 (2012) 369–377, https://doi.org/10.1016/j.matdes.2012.06.032.

[25] S. Mahabunphachai, M. Koç, Investigations on forming of aluminum 5052 and 6061 sheet alloys at warm temperatures, Mater. Des. 31 (2010) 2422–2434, https://doi.org/10.1016/j.matdes.2009.11.053.

[26] P.T. Summers, Y. Chen, C.M. Rippe, B. Allen, A.P. Mouritz, S.W. Case, et al., Overview of aluminum alloy mechanical properties during and after fires, Fire Sci. Rev. 4 (2015), https://doi.org/10.1186/s40038-015-0007-5.

[27] E. Fagerholt, D. Morin, V. Aune, T. Børvik, O.S. Hopperstad, Using DIC-based FEM to determine work-hardening parameters in structural steels, Adv. Model Simul. Eng. Sci. 12 (2025) 18, https://doi.org/10.1186/s40323-025-00292-8.

[28] L.P. Luong, G. Alonso Aruffo, R. Bonnaire, L. Penazzi, Evaluation of an improved filtering method for strain measurement at high temperatures using 2D-DIC, Experiment. Mec. 65 (6) (2025) 927–941, https://doi.org/10.1007/S11340-025-01174-1.

[29] Tayon WA, Mulvaney MC, Stegall DE, Hochhalter JD. Assessing flow formability of aerospace aluminum alloys via DIC tensile testing 2023.